Chapter 3. The Conventional Axial Mode Helix Antenna

3.1 Introduction

In this chapter we examine the conventional axial mode helix and its operation. Through an exploration of the conventional axial mode helix, we gain insights into the operation of axial mode structures that support circular polarization and lay the groundwork for understanding the operation of the Stub Loaded Helix (SLH) antenna. In this chapter we also examine the performance behavior of the axial mode helix which will provide benchmarks against which the performance of the SLH can be compared.

3.2 Conventional Helix Geometry

Figure 3.1 shows the geometry for a conventional axial mode helix, repeated from Chapter 2 for convenience. The defining parameters of the conventional helix are the helix diameter, D, the helix circumference, C, the turn-to-turn spacing, S, the pitch angle of the turns, α, and the axial length, A. The diameter, and hence circumference, primarily determine the frequency of operation of the helix. The circumference of the helix is approximately equal to one wavelength at the center frequency of operation of the helix.

Not shown in Figure 3.1 is the groundplane and feed details of the helix. The helix is usually mounted above the groundplane at the feed end of the helix with the groundplane perpendicular to the axis of the helix as shown in Figure 3.2. The groundplane can be any shape, but is typically square or round with a diameter of one-half to one wavelength. Other groundplane configurations may be used, for example the conical reflector of the helicone shown in Chapter 2. For our discussions we will only consider the conventional axial mode helix with a flat groundplane.

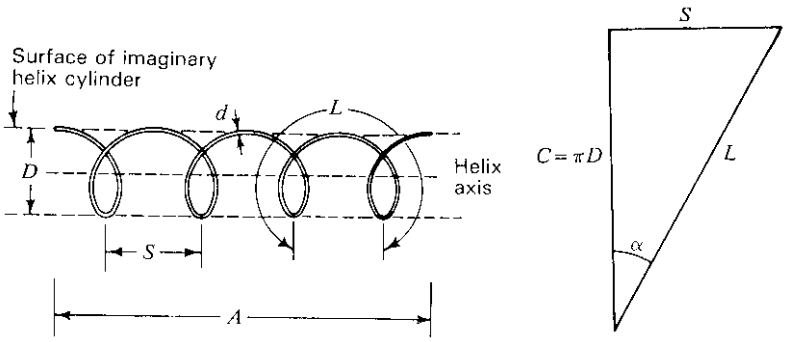

(a) (b)

Figure 3.1 Basic helix geometry defining diameter (D), turn-to-turn spacing (S), axial length (A), circumference (C), turn length (L), and pitch angle (α). In (b) the relationships between S, C, D, L and α are shown for a single turn that has been stretched out flat. [Kraus, 1988]

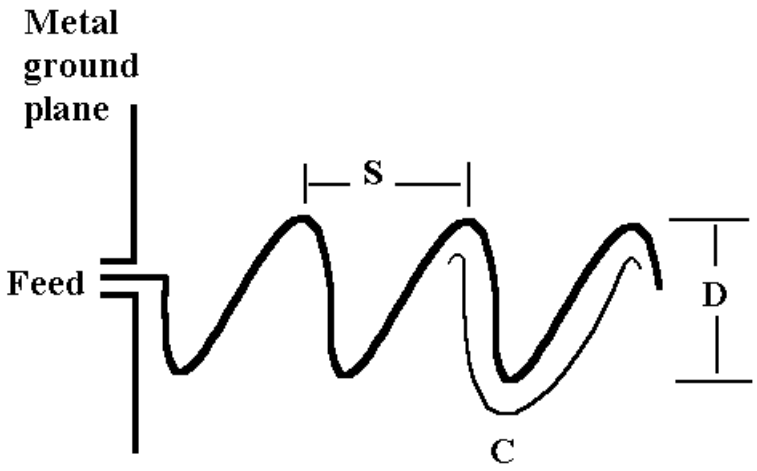

Figure 3.2 Conventional axial mode helix showing the feed and groundplane

3.3 Operating Principles for the Axial Mode Helix Antenna

Kraus [1988] discovered axial mode operation occurs when the circumference, C, of the helix is approximately one wavelength at the center frequency of operation and endfire axial mode operation is supported for approximately $0.75\lambda < C < 1.3\lambda$. The optimal pitch angle, α, was found to be approximately $10° < \alpha < 20°$ for axial mode operation. This corresponds to a inter-turn spacing of $0.17\lambda < S < 0.36\lambda$ at the center frequency of

operation. The axial-mode helix's primary attributes are that it produces circular polarization and moderate gain over a wide (~50%) bandwidth. The purpose of this discussion is to review the operating principles of how the axial mode helix operates. In particular, this discussion centers on how the current modes and phasing on the helix conductor affect the helix's properties.

To a first approximation, the helix can be considered to be a continuous linear antenna carrying a traveling wave. Since the helical winding is periodic with a period equal to the turn spacing, the helix can be considered to be a periodic structure, allowing us to borrow analytical tools developed for more generalized periodic structures.

Consider the linear array of *n* isotropic point sources with equal amplitude and spacing shown in Figure 3.3. The phase difference of the fields from adjacent sources as observed in the far field is given by [Kraus, 1988]

$$\psi = \frac{2\pi}{\lambda_0} S \cos\phi - \delta = \beta_0 S \cos\phi - \delta \tag{3-1}$$

where S = spacing between sources, m
λ_0 = free space wavelength, m
ϕ = angle between array axis and observation point, rad.
δ = relative phase difference between sources, rad.
β_0 = free space phase constant

For the endfire case, $\phi = 0$, linear array theory shows this corresponds to $\delta = \pm \beta_0 S$ [Kraus, 1988]. If the spacing, S, is a half-wavelength there will be two endfire lobes (0°, 180°). In order to eliminate the unwanted lobe, the spacing must be reduced below a half-wavelength. It can be shown that for the ordinary endfire case the condition on the spacing is given by [Stutzman and Thiele, 1981]

$$S \leq \frac{\lambda}{2}\left(1 - \frac{1}{2n}\right) \tag{3-2}$$

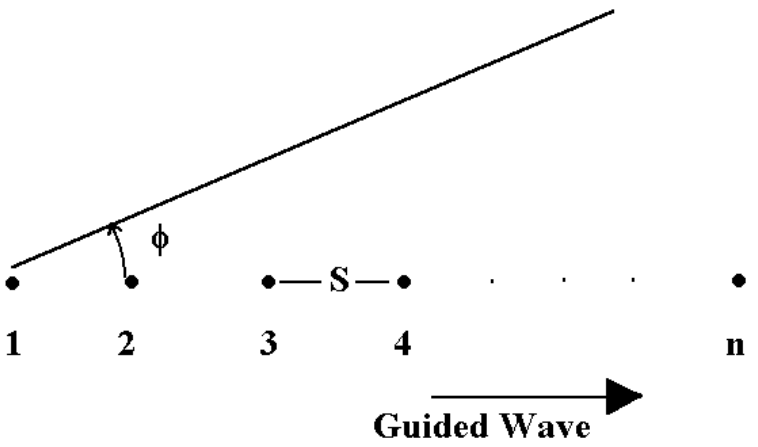

Figure 3.3 Linear array model for an n-turn axial-mode helix antenna consisting of n point sources with equal spacing, S, and amplitudes.

The directivity of a linear array can be increased over that of the ordinary endfire case if the interelement phase, δ, is increased. This is given by the Hansen-Woodyard condition for increased directivity where [Stutzman and Thiele, 1981]

$$\delta = \pm\left(\beta_0 S + \frac{\pi}{n}\right) \tag{3-3}$$

In order to prevent the back lobe from becoming as large or larger than the main lobe, Hansen-Woodyard also places a restriction on the spacing between elements such that [Stutzman and Thiele, 1981]

$$S < \frac{\lambda}{2}\left(1 - \frac{1}{n}\right) \tag{3-4}$$

The Hansen-Woodyard condition illustrates the necessary requirements for maximum endfire directivity for a linear array, namely the requirements for interelement phasing and spacing. It is of limited usefulness in considering a periodic structure such as the axial mode helix since only one mode of operation is considered. Instead a more generalized approach is required.

If we assume that the array is a periodic structure supporting a traveling wave traveling from left to right along the array, the phase constant, β, of the traveling wave can be given by [Kraus, 1981]

$$\beta = \frac{2\pi}{\lambda_0 p} \qquad (rad\ m^{-1}) \tag{3-5}$$

where $p = v/c$ = relative phase velocity, dimensionless
v = wave velocity, m s^{-1}
c = velocity of light, m s^{-1}

The phase difference between sources is thus given by [Kraus, 1981]

$$\delta = \frac{2\pi}{\lambda_0 p} S \qquad (rad) \tag{3-6}$$

For the fields from the n sources to be in-phase at a distant point it is required that [Kraus, 1981]

$$\psi = 2\pi m \qquad (rad) \tag{3-7}$$

where m = mode number = $0, \pm 1, \pm 2$, etc.

Substituting equations (3-1) and (3-6) into (3-7) we obtain [Kraus, 1981]

$$2\pi m = \beta_0 S \cos\phi - \beta S \tag{3-8}$$

where $\beta_0 S$ = electrical distance between sources for a free-space wave, rad
βS = electrical distance between sources for the guided wave, rad

For the periodic structure there are now three parameters that determine the angle of the beam maximum: the mode number, m, the element spacing, S, and the relative phase velocity of the guided wave, p. Thus, for a given periodic structure with spacing, S, there are mathematically an infinite number of modes, with corresponding guided phase velocities, that have a beam maximum in the direction of ϕ. However, not all of these modes are realizable since the guided phase velocity to support the mode may not be realizable.

As an example consider a structure with a spacing $S = \frac{\lambda}{4}$. For the endfire case, $cos\ \phi = 1$, the values of the relative phase velocity for the guided wave, p, for several modes are given in Table 3.1.

Table 3.1 Relative phase velocity for different modes with S=$\frac{\lambda}{4}$

mode number, m	relative guided phase velocity, p
0	1
-1	1/5
1	-1/3
-2	1/8
2	-1/7

From Table 3.1 it is obvious that the m = 1 and m = 2 modes cannot be realized. For this structure no positive mode numbers can be supported.

A more common way of analyzing periodic structure is to plot the electrical spacing, $\beta_0 S$, of the free space wavelength versus the electrical spacing, βS, of the guided wave along the array. These quantities are usually normalized by 2π so that the plot is of S/λ versus $S/p\lambda$, or more commonly referred to as a k-β diagram. This is also termed a Brillouin diagram [Brillouin, 1946] and is a useful tool for illustrating which modes are propagating on a structure. This is particularly useful in analyzing helical antenna structures since the helix supports several current modes on its structure.

For example, Sensiper [1955] describes how a helix supports more than one current mode. Sensiper analyzed a sheath model for the helix in which the helix is modeled by an anisotropic current conducting sheet. Solving for solutions of the determinantal equation of the sheath helix, he showed a solution for the n = 1 mode in addition to the n = 0 mode which was previously known. The k-β diagram for his solution is shown in Figure 3.4. In this figure the phase velocity of the wave is given by the slope of the straight line drawn for the origin to a point on the curve. The group velocity is given by the slope of the curve at that point.

Mathematically, it can be shown that a helical structure will support more than one current mode, but there is also experimental evidence to support this conclusion. In some of the earliest measurements on axial mode helices by Kraus and Williamson [1948], it became

evident that the current distribution on the helix structure was complex. Figure 3.5 shows measured current distributions along a helix for two different frequencies as reported by Kraus and Williamson [1948]. The upper plot in Figure 3.5 shows the current distribution along the helix at a frequency where the helix does not radiate a circularly polarized wave. The lower plot is for a frequency where the radiation is circularly polarized.

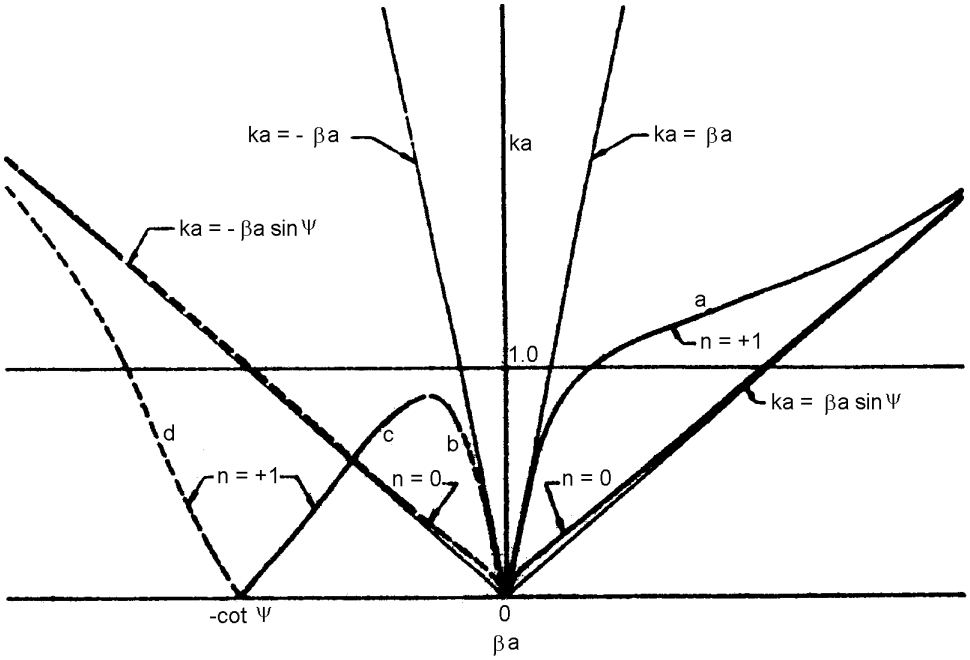

Figure 3.4 Solutions of the sheath determinantal equation, ka vs βa for n = 0, 1, 90° < ψ < 0° [Sensiper, 1955].

Kraus uses these current distributions to attribute the axial mode helix operation to the presence of four traveling waves; an unattenuated wave and an exponentially attenuated wave traveling in each direction as illustrated in Figure 3.6. The unattenuated and exponentially attenuated wave, 1 and 2 in Figure 3.6, are launched from the feed end of the helix. Both traveling waves propagate along the helix until they reach the open end of the helix winding. At this end, they are reflected forming the two backward traveling waves, 3 and 4 in Figure 3.6. Interference between these four traveling waves create the current distributions shown in Figure 3.5.

The upper plot in Figure 3.5 shows a standing wave pattern that is created when only the two unattenuated waves, 2 and 4, propagate along the helix. This occurs in the region of operation where the axial mode helix does not generate a circularly polarized wave. When

the helix supports propagation of both the unattenuated and exponentially attenuated waves, the result is a current distribution such as the lower plot of Figure 3.5. Also, for this mode of operation, the magnitude of the exponentially attenuated wave is larger than the unattenuated wave.

Table 3.2 Design Parameters for the Helix Results in Figure 3.5 [Kraus and Williamson, 1948]

C, circumference	70.68 cm
D, diameter	22.5 cm
α, pitch angle	12°
S, turn-to-turn spacing	15 cm
N, # turns	7
L, axial length	112 cm
Groundplane dia.	66 cm

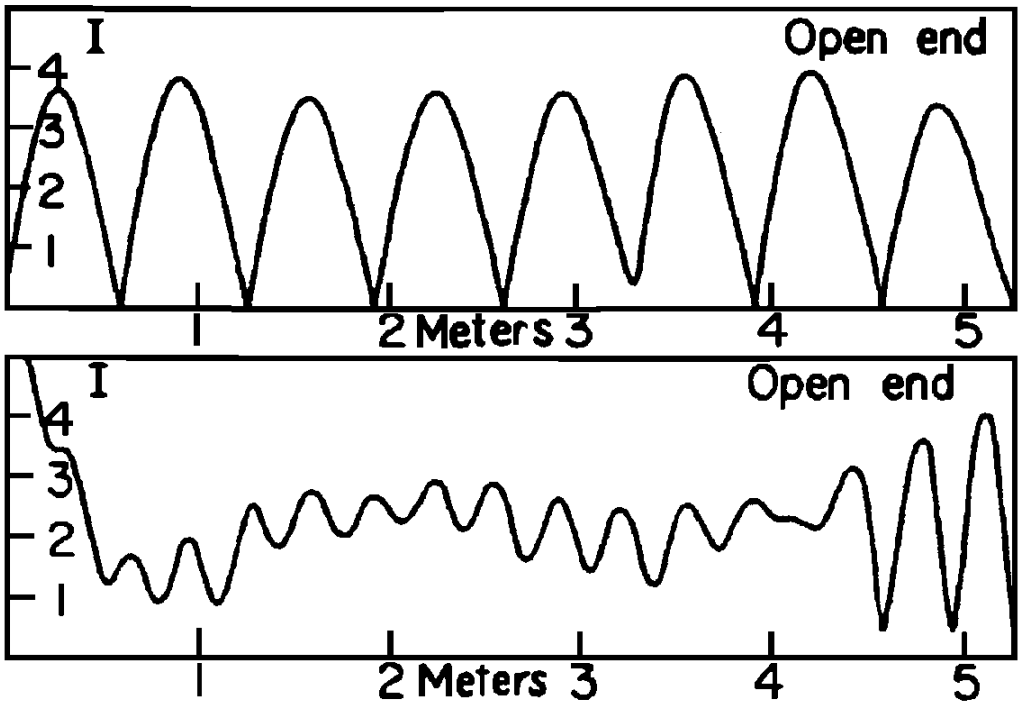

Figure 3.5. Measured current distributions on a helix at 250 MHz (upper) and 450 MHz (lower) for the helix specified in Table 3.2 [Kraus and Williamson, 1948]

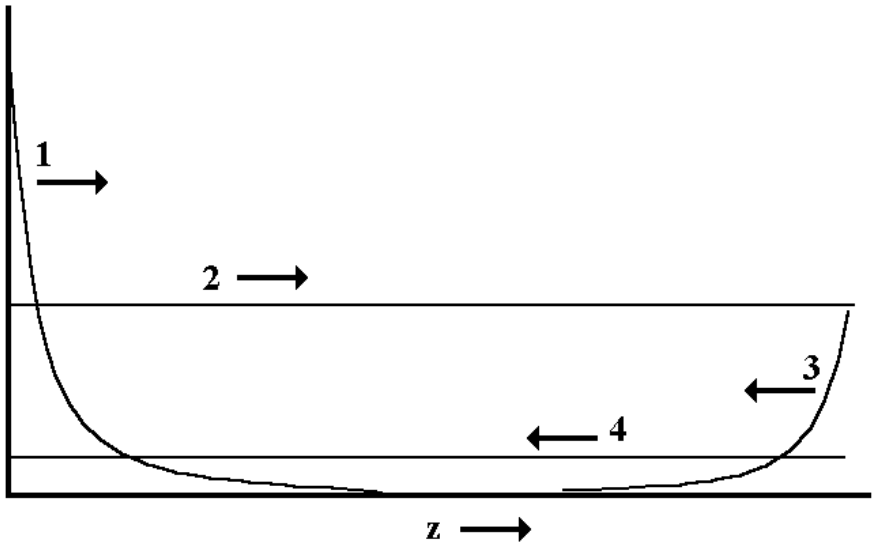

Figure 3.6. Illustrative current amplitude distributions of traveling waves supported on an axial-mode helix. With the feed at the left hand side of the graph, 1 represents an exponentially decaying forward traveling wave, 2 represents an unattenuated forward traveling wave, 3 represents an exponentially decaying reverse traveling wave generated by the reflection at the end of the helix, and 4 represents an unattenuated reverse traveling wave generated by the reflection at the end of the helix. After [Kraus and Williamson, 1948].

Kraus and Williamson [1948] suggest that anytime a traveling wave is supported on a helix, a circularly polarized wave is radiated. However, the backwards traveling wave resulting from the reflection at the open end of the helix results in a circular wave of the opposite sense also being radiated. This explains why the helix would not radiate a circularly polarized wave for the case of the upper plot shown in Figure 3.5 because the forward and backward traveling waves are approximately the same amplitude, resulting in two opposite sense circularly polarized waves being radiated in the forward direction. Clearly for circular polarization to occur, it is necessary that the reflected waves from the open end of the helix be significantly attenuated relative to the forward traveling wave.

In the work by Kraus and Williamson [1948], they reported measurements of the phase velocity of the traveling waves along the helix shown in Figure 3.7. Figure 3.7 shows that the phase velocity is approximately equal to the speed of light, c, at low frequencies. At a certain point the phase velocity exhibits a sudden drop to less than c, indicating the presence of a slow wave on the helix. There is a gradual increase in the phase velocity

with frequency back toward c. This region of slow phase velocity corresponds to the operating frequencies at which the helix will produce circular polarization. Hence, it appears that a slow wave condition is necessary for axial mode operation with circular polarization.

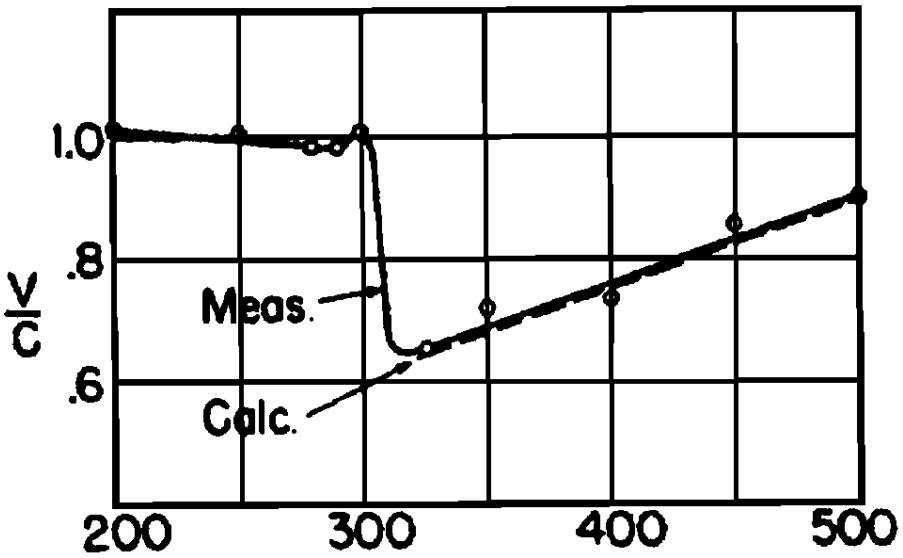

Figure 3.7. Measured and calculated phase velocity ratio of helix as a function of frequency in MHz. [Kraus and Williamson, 1948].

The phase velocity measurements by Kraus and Williamson [1948] seem to imply that all the traveling waves are slow waves in the operational frequency region of the helix. However, a more extensive measurement campaign by Marsh [1951] reached a different conclusion. Marsh made current distribution measurements of a uniform circular helix over a wide bandwidth including below and above the operating frequency range of the axial mode of operation. In explaining the helix current distributions and radiation characteristics, Marsh used multiple traveling waves much like Kraus and Williamson, as illustrated in Figure 3.6, but he applied them to a mode distribution concept. Marsh defined three mode distributions T_0, T_1, and T_2 which describe the currents and waves supported by the helix. The three mode distributions correspond to the frequency regions below where circularly polarized radiation is supported (T_0), where endfire circularly polarized radiation is supported (T_1) and above where endfire circularly polarized radiation is supported (T_2).

The T_0 mode predominates when the helix circumference $C < 0.675\lambda$. The T_0 traveling waves experience little attenuation as they travel down the helix and they propagate with a phase velocity equal to the speed of light, c. The result is a large standing wave pattern such as shown in the upper plot of Figure 3.5. The T_0 mode waves correspond to the unattenuated waves 2 and 4 shown in Figure 3.6. Marsh, like Kraus and Williamson, showed that these waves propagate with a velocity of c. These modes radiate very poorly.

The T_1 mode currents occur for a helix circumference of $0.8\lambda < C < 1.3\lambda$ [Marsh, 1951]. The T_1 mode currents are decaying amplitude waves, similar to the exponentially attenuated waves 1 and 3 shown in Figure 3.6. Marsh shows that the T_1 mode currents propagate at a phase velocity that is less than c and is frequency dependent as shown in Figure 3.8 [Marsh, 1951]. T_0 mode currents also are present on the helix when T_1 mode currents predominate but their amplitude is much less than that of the T_1 currents. This is the operating region which produces endfire circularly polarized radiation.

The endfire radiation of an axial mode helix is the result of the presence of two different current traveling wave modes supported by the helix's periodic structure: an unattenuated current mode with a phase velocity of c, and an exponentially decaying current mode with a phase velocity less than c. Each of these waves is launched from the feed end of the helix. At the open end of the helix, both modes experience a reflection that generates an equivalent backward traveling wave of lower amplitude along the helix. The radiation pattern and axial ratio of the antenna is the a function of the resultant fields produced by these four waves.

In Marsh's analysis, the endfire radiation is explained by traveling waves of two current modes, T_0 and T_1, but one current mode has a phase velocity of c and the other has is a slow wave with a phase velocity less than c. This is the key difference between the analysis of Marsh and that of Kraus and Williamson.

Marsh defines a third current mode called the T_2 mode which occurs when $C > 1.3\lambda$. The T_2 current mode is also an exponentially decaying wave but it does not decay as rapidly as the T_1 mode wave does and it has a slower phase velocity than the T_1 mode as shown in Figure 3.6 In the region of operation where the T_2 mode is supported the helix antenna pattern has broken up into a large number of lobes. Therefore, there has been little interest in investigating this mode.

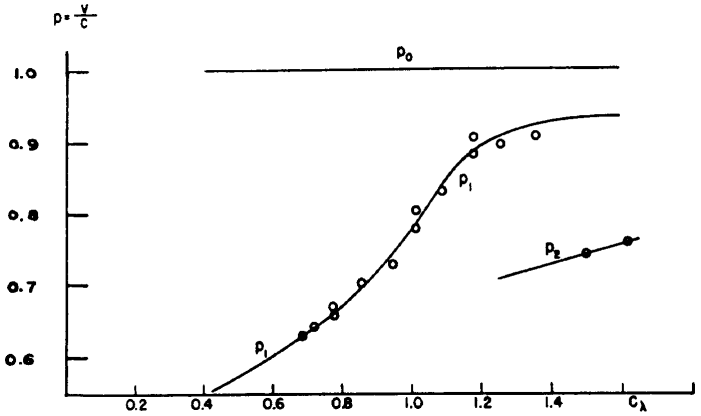

Figure 3.8. Relative phase velocity, p, versus relative circumference, C_λ, for the T_0, T_1, and T_2 modes on the helix [Marsh, 1951].

3.4 Simulation of Conventional Helix Antenna

3.4.1 Simulation of Conventional Helix Antenna Currents

In order to understand the operation of both conventional axial modes helices, as well as the Stub Loaded Helix, NEC, the Numerical Electromagnetics Code, was used to model the currents on a conventional axial mode helix. The design parameters for the axial mode helix used in these following simulations are given in Table 3.3. All simulations assumed an infinite groundplane.

The center frequency of operation, f_c, for the helix was nominally 300 MHz, because the helix circumference, C, was fixed at 1 m. NEC simulations were performed for this antenna at frequencies of 200, 300, and 400 MHz, corresponding to 0.66 f_c, f_c, and 1.33 f_c. By examining operation at these frequencies, we can observe the behavior of the helix current for the different modes that can be supported on the structure using the currents predicted by NEC.

Table 3.3 Design parameters of NEC simulated full size axial mode helix

C, circumference	1 m
f_c , center frequency	300 MHz
α, pitch angle	13°
N, number of turns	10
L, axial length	2.31 m

Figure 3.9 shows the NEC results of the current magnitude and phase for the full size helix at a frequency of 0.66 f_c (200 MHz) where the circumference is slightly below the normal axial mode operating range. The current along the helix is plotted as a function of axial length along the helix in Figure 3.9(a), . The current magnitude indicates a standing wave along the helical winding that is very similar to Kraus' measured results shown in Figure 3.5. This is a region in which the helix does not support a circularly polarized wave. The current on the helix is essentially a superposition of unattenuated forward and a reverse traveling waves along the structure.

The phase of the current along the helix is shown in Figure 3.9(b). The current phase is very nonlinear in its progression. There are abrupt, almost step, changes in the current phase that correspond to the nulls in the current magnitude. Also plotted along with the simulated helix current phase is the corresponding Hansen-Woodyard phase condition for this structure. It is obvious that the current phasing differs markedly from the Hansen-Woodyard condition. This is most likely due to the a combination of strong interaction of the forward and reverse traveling waves on the structure and geometry of the helix. In Figure 3.9(a), the standing wave pattern of the current magnitude indicates that both forward and reverse traveling waves have comparable amplitudes. The result is that the phase of the reflected wave has a significant impact on the vector sum of the forward and reflected waves.

Additionally, the geometry of the helix has an impact on the spatial phasing of the currents on the helix. The circumferntial turn length is small relative to the wavelength for the results in Figure 3.9 where C = 0.677 λ at 200 MHz. The result is that the spatial phasing due to the turn length and pitch angle are such that the currents on the helix deviate significantly from the Hansen-Woodyard condition.

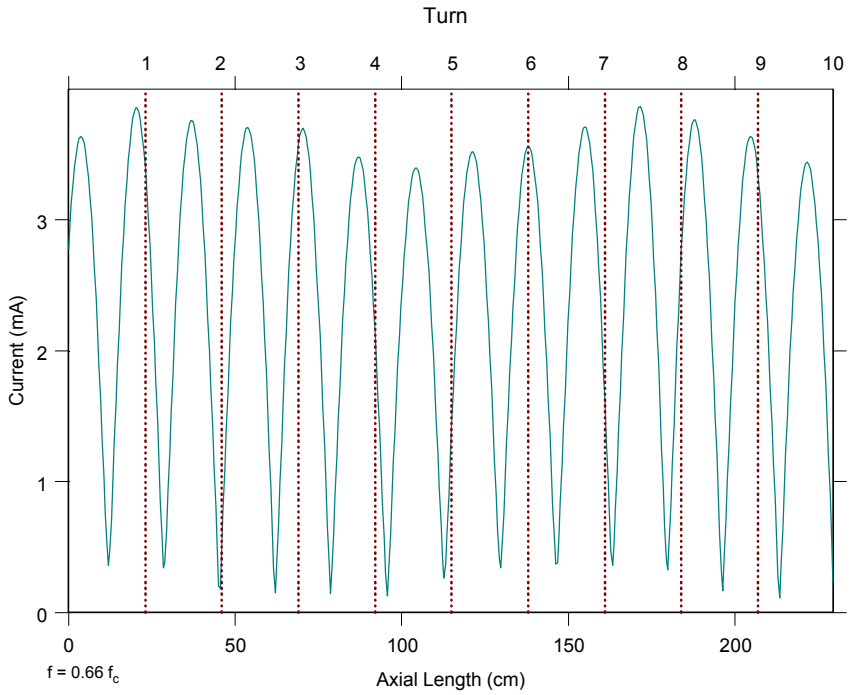

(a)

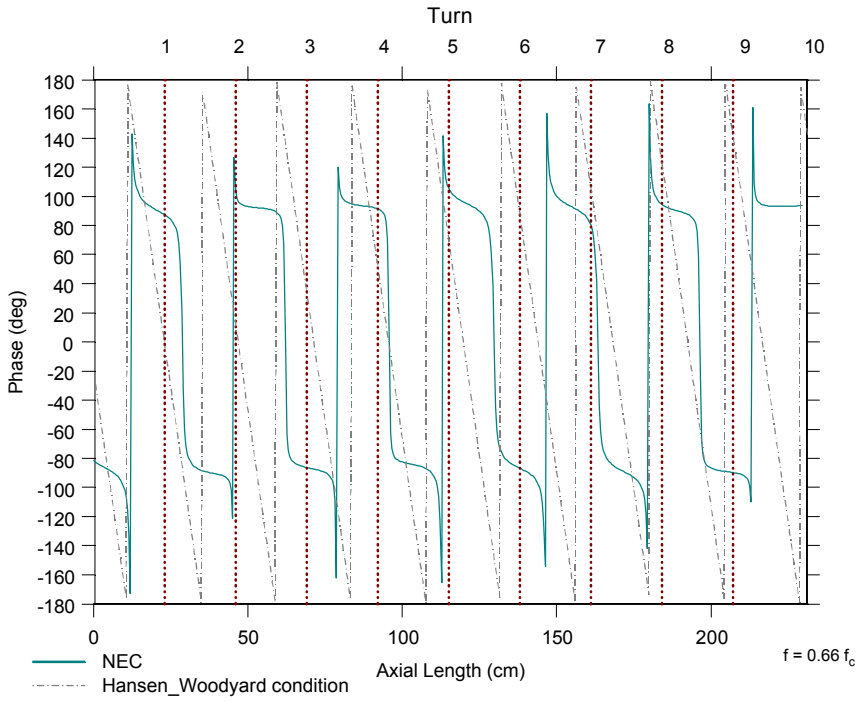

(b)

Figure 3.9 NEC simulation of current magnitude and phase along a conventional helix of Table 3.3 at $f = 0.66\ f_c$ ($C = 0.66\ \lambda_c$), $f = 200$ MHz. Vertical dashed lines indicate boundaries between turns.

Figure 3.10 shows the NEC simulation results for the conventional helix at 300 MHz, f_c, the center frequency of operation for the full size helix where C = λ_c. The current magnitude shown in Figure 3.10(a), shows an initial decay of current from the feedpoint. This is followed by a slight increase in magnitude, which then settles down to gradual rippling decay. At the end of the helix we see a region of small standing waves, much like in Figure 3.9(a). This region at the end of the helix is where the forward traveling wave is reflected from the end of the helix to create a reverse traveling wave. The interaction of these two waves of comparable amplitudes, results in the standing wave pattern.

The increase in current amplitude centered around turn 3 can also be explained by an interaction between forward and reverse traveling waves as well. In this region, the waves interfere constructively at turn 3, but destructively at the ends of turns 2 and 5.

The results in Figure 3.10(a) at 300 MHz (f_c) are qualitatively comparable to Kraus' results shown in Figure 3.5 for his helix at 450 MHz. This approximately exponential decay of the helix current along its axis is indicative of the structure supporting a circularly polarized wave.

The current phase shown in Figure 3.10(b) indicates an almost linear phase taper along the helix, except at the last turn or two. At the end, of course, there is the strong interaction of the forward and reverse traveling waves, resulting in the standing wave pattern seen in the current magnitude and the nonlinear phase progression.

The Hansen-Woodyard condition is also plotted in Figure 3.10(b). It should be noted that the current phase along the helix closely matches the Hansen-Woodyard condition over most of the helix length. The greatest deviation from the Hansen-Woodyard condition occurs at the end of the helix, as might be expected. At the end of the helix, the reflected, or reverse traveling, wave has its greatest amplitude. Thus, its impact on the vector sum of the forward and reverse traveling currents is greatest. As the reverse traveling wave propagates back toward the feed end of the helix, it is attenuated as a result of radiation. Thus, it could be argued that almost all of the variation from the Hansen-Woodyard condition could be explained as a result of interaction of the forward traveling wave with the reverse traveling wave.

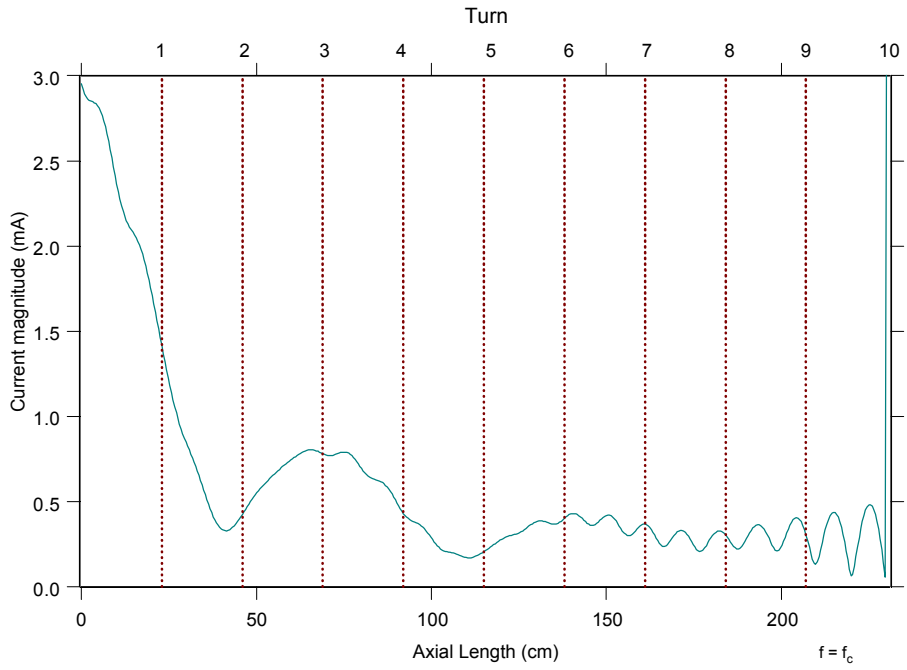

(a)

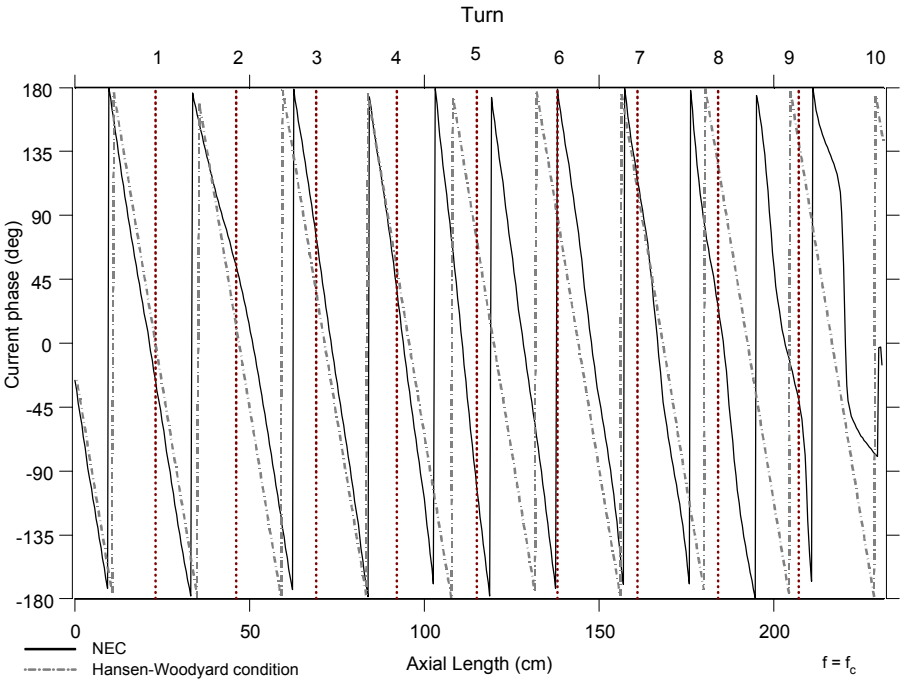

(b)

Figure 3.10 NEC simulation of current magnitude and phase along a conventional helix of Table 3.3 at $f = f_c$ ($C = \lambda_c$), $f = 300$ MHz. Vertical dashed lines indicate boundaries between turns. In (b) the Hansen-Woodyard phase condition is also indicated.

Figure 3.11 shows the NEC simulation results for the helix in Table 3.3 modeled at 400 MHz, or 1.33 f_c ($C = 1.33\ \lambda_c$). The current magnitude along the helix length is shown in Figure 3.11(a). It has the appearance of a superposition of two standing wave patterns, one with a short period and one with a long period. As in the previous results shown in Figure 3.9, we conclude that this pattern is the product of interaction between forward and reverse traveling waves of comparable amplitudes. It would appear that for frequencies far above the center frequency of the helix, there is the appearance of another mode on the helix as identified by Marsh [1951] as the T_2 current mode.

The simulated helix current phase is shown in Figure 3.11(b). The phase progression along the helix is quite non-linear, similar to the previous case shown in Figure 3.9. Again, the Hansen-Woodyard condition is plotted on the same graph as the helix current phase. The variation of the simulated helix current phase from the Hansen-Woodyard condition is significant.

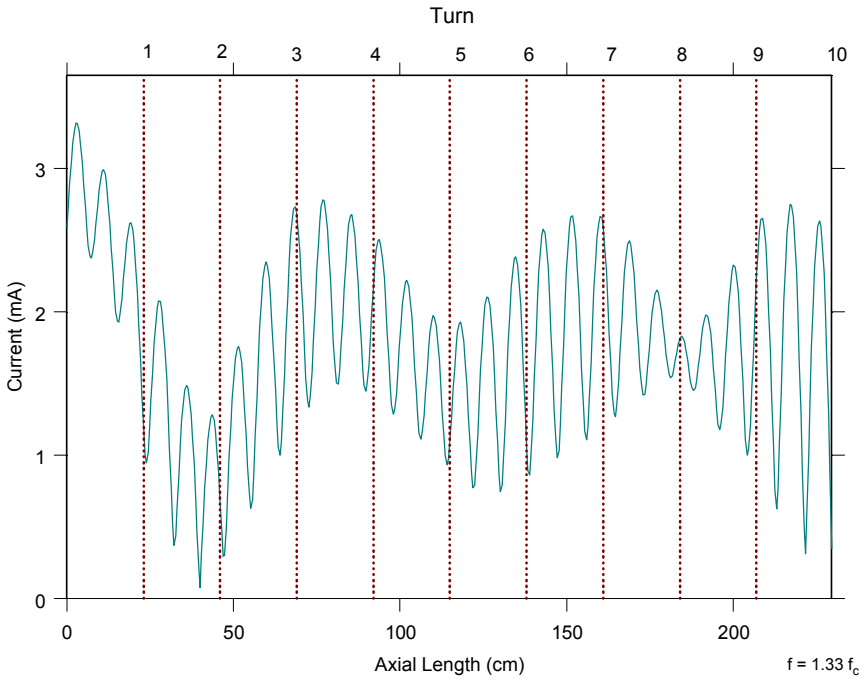

(a)

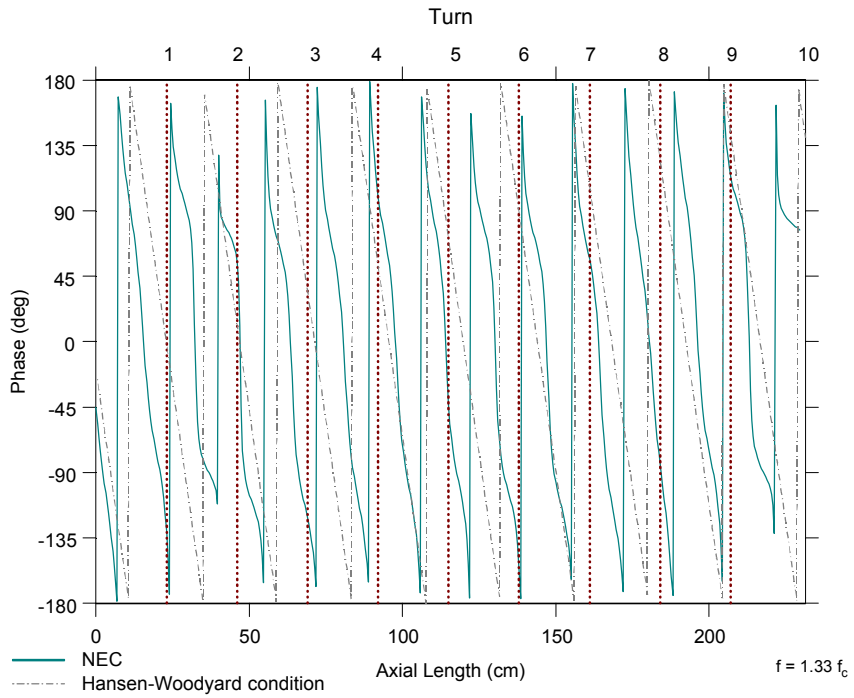

(b)

Figure 3.11 NEC simulation of current magnitude and phase along a conventional helix of Table 3.1 at f = 1.33 f_c (C = 1.33 λ_c). Vertical dashed lines indicate boundaries between turns.

Figure 3.12 shows the NEC predicted patterns for three cases discussed above. Figure 3.13 shows the NEC predicted axial ratio for the three cases. The patterns shown for frequencies of 0.66 f_c and f_c in Figure 3.12(a) and (b), are typical of patterns expected for an axial mode helix. Although the pattern in Figure 3.12(a) appears fairly normal, the axial ratio is poor as seen in Figure 3.13. In Figure 3.12(c), the pattern for the f = 1.33 f_c (C = 1.33 λ_c) case is starting to show splitting in the main lobe of the pattern. This is indicative of higher order modes being excited on the helix. As Figure 3.13 shows, the axial ratio has also deteriorated.

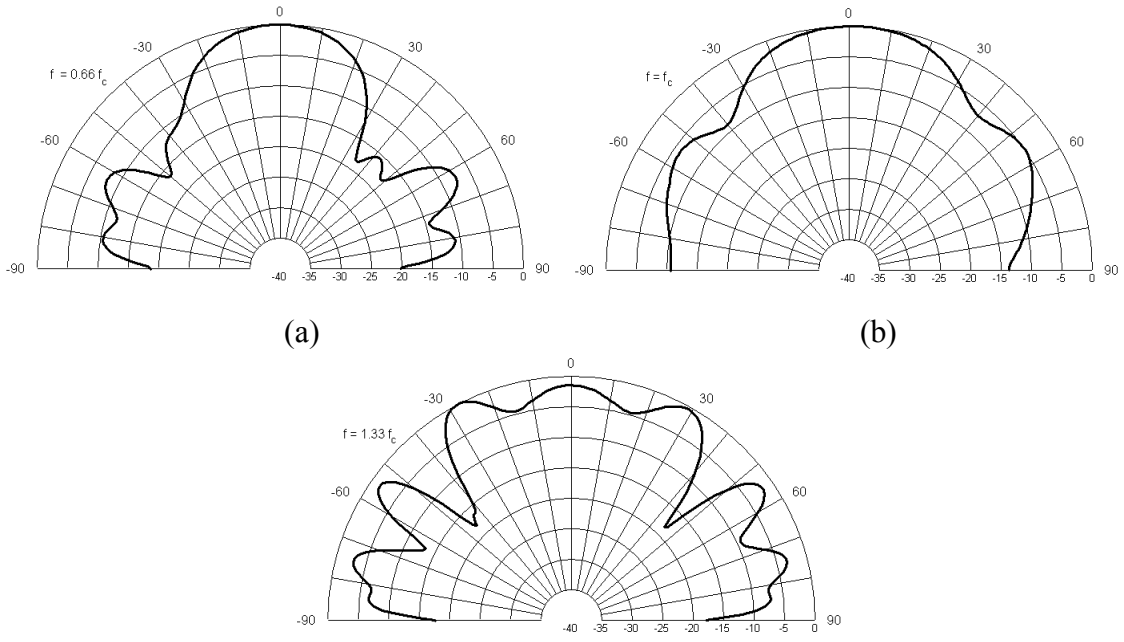

Figure 3.12 NEC simulated normalized patterns for the full size helix of Table 3.3 at (a) 0.66 f_c, (b) f_c, and (c) 1.33 f_c.

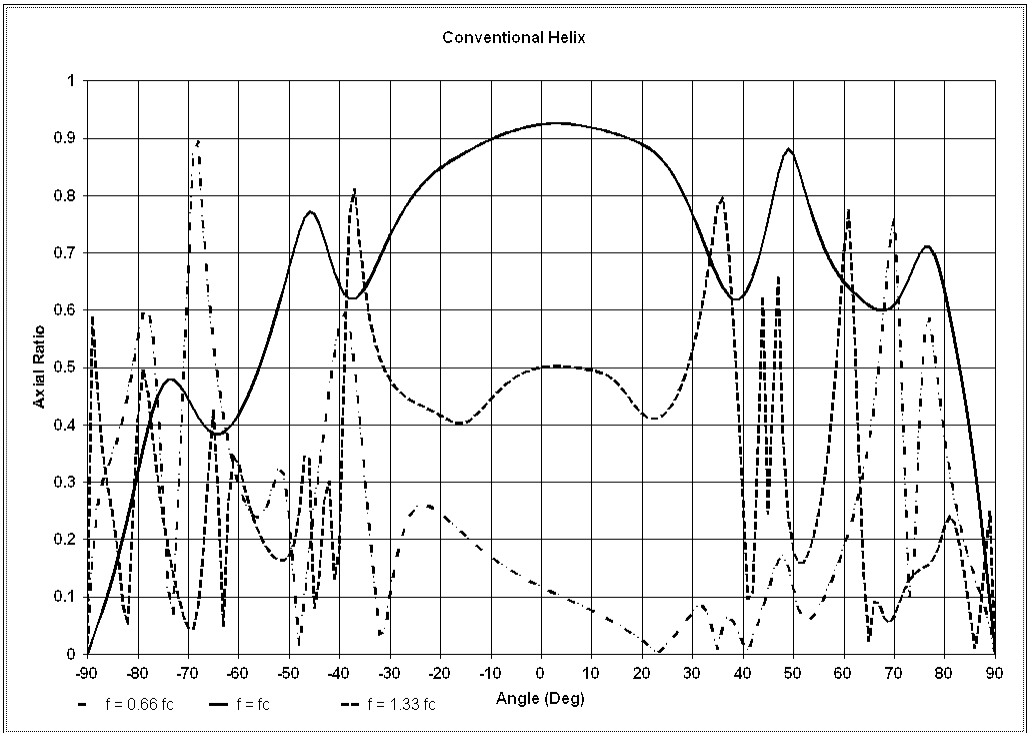

Figure 3.13 NEC simulated axial ratios as a function of pattern angle for the full size helix of Table 3.3 at frequencies of 0.66 f_c, f_c, and 1.33 f_c (C = 0.66 λ_c, λ_c, 1.33 λ_c).

3.4.2 Simulation of Conventional Helix Performance

There have been numerous studies of the performance capabilities of the conventional helix antenna over the years. They have been empirical [King & Wong, 1980], theoretical [Lee, et al., 1982], and numerical [Emerson, 1994]. These studies have primarily addressed the issue of boresight gain as a function of helix diameter, length, and pitch. The conclusions from these different studies are not in complete agreement.

What is probably considered the classic experimental study of helix performance is the work of King and Wong [1980] who made an extensive series of gain and pattern measurements on conventional helices of varying lengths and across a wide bandwidth. Figure 3.14 is a graph from their results showing the gain of a conventional axial mode helix as a function of helix length and circumference. These results are usually considered the standard by which other results, theoretical and numerical, are compared. While the work of King and Wong is excellent, the comparisons with these results shows poor agreement, as we shall see.

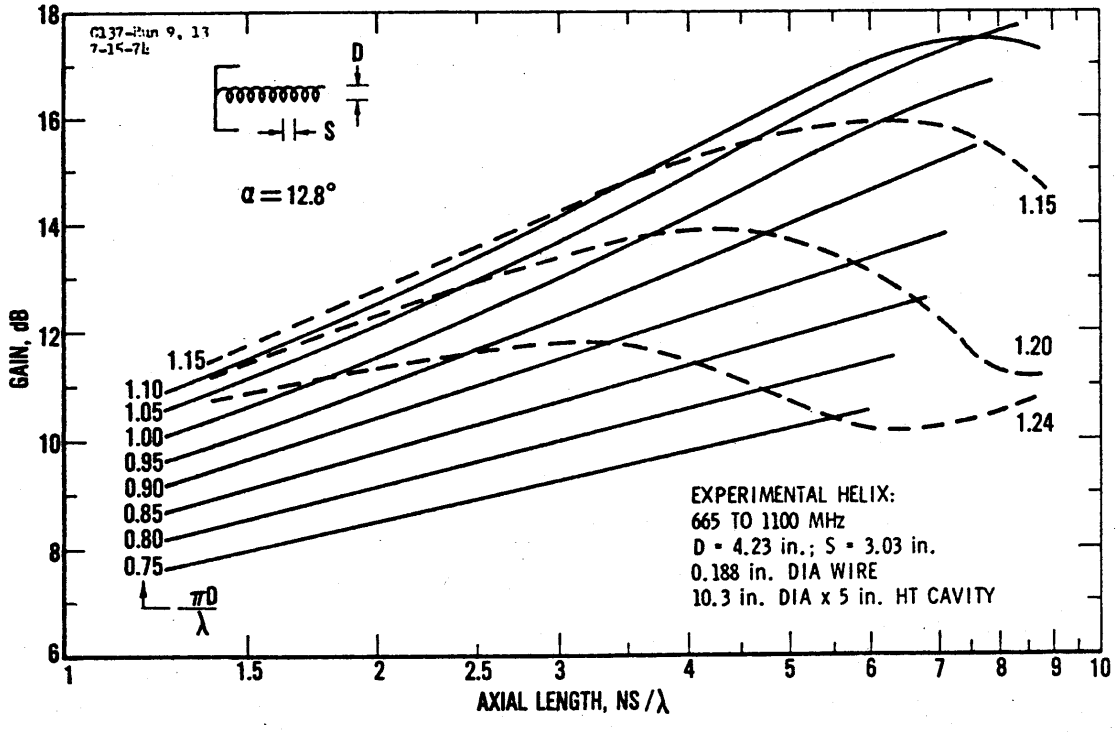

Figure 3.14 Measured gain versus axial length of a conventional axial mode helix as a function of helix circumference. [King and Wong, 1980]

Emerson [1994, 1995] conducted an extensive modeling campaign using NEC2 (Numerical Electromagnetics Code) to explore the design space of the conventional helix antenna with respect to gain and axial ratio. His study explored the effects of turn diameter, spacing and axial length on boresight gain, axial ratio and input impedance. Figure 3.15 shows a comparison of the gain versus turn radius as measured by King and Wong and simulated by Emerson. From Figure 3.15, it is obvious that the gain values predicted by Emerson's models are less than those measured by King and Wong. The differences are typically 1 - 2 dB, a fairly significant amount.

Figure 3.16 is a graph from Emerson's [1995] work that shows the peak helix gain as a function of axial length. For comparison, the measurements of King and Wong, and the theoretical results of Lee and Wong are shown with Emerson's results. From these results, it is obvious that there are significant differences between both the theoretical results of Lee and Wong [1982] and Emerson's simulation results, both underestimating the measured gains of King and Wong.

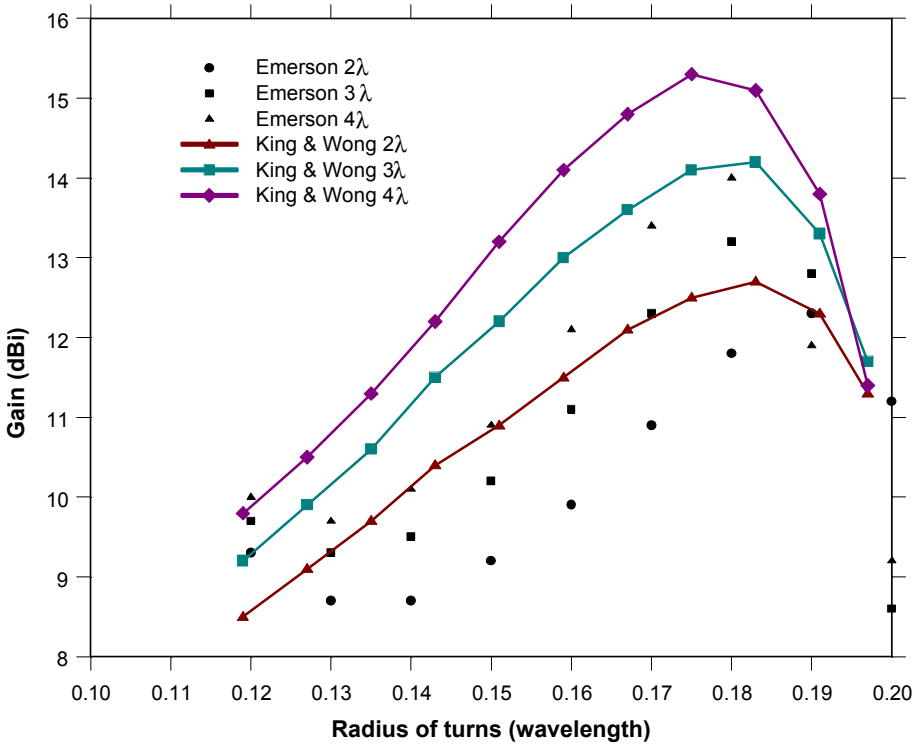

Figure 3.15 Comparison of gain versus helix radius for conventional helices of 2, 3, and 4 wavelengths axial length as measured by King and Wong [1980] and modeled by Emerson [1994].

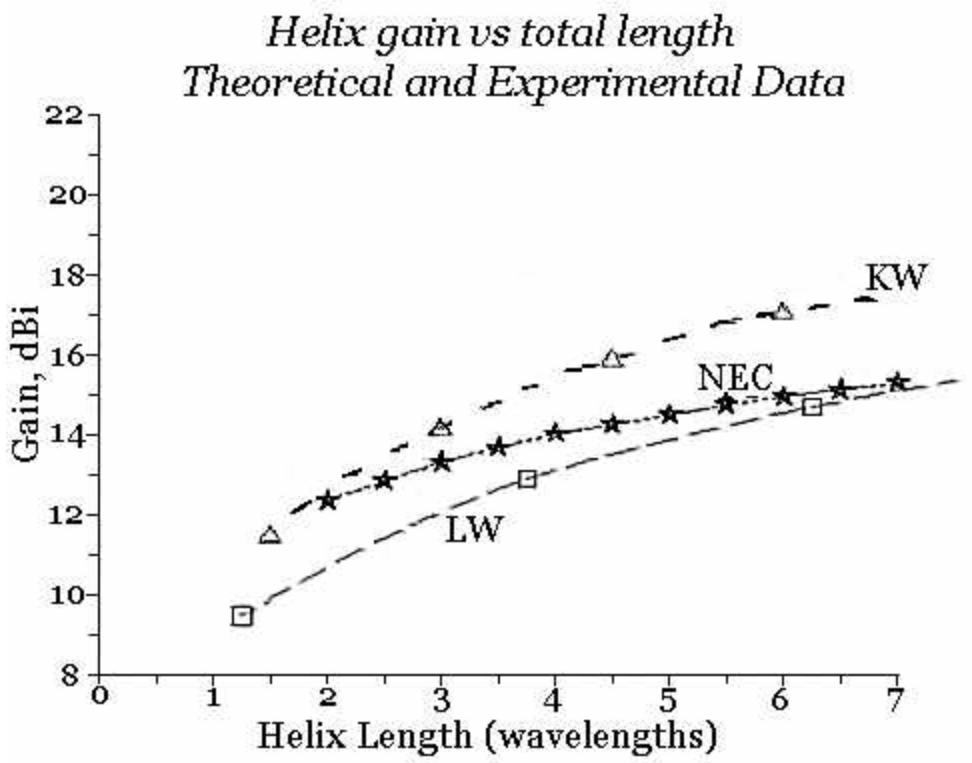

Figure 3.16 The peak gain of a helix antenna as a function of its length as determined by the following methods: KW (dashes & triangles) measurements of King and Wong; NEC (short dashes & stars) simulation by Emerson; LW (long dashes & squares) theoretical gain from Lee and Wong. [Emerson, 1995]

The large differences between the various gain values in Figure 3.16 obtained by measurement, simulation and theory are disturbing. There is, however, an explanation for at least some of the differences that we now present.

Figure 3.14 shows the results of King and Wong's measurements along with a description of their experimental test article. The helix that King and Wong built used a cup reflector backing the helix rather than a flat plate reflector. A cup reflector can have a significant effect on the helix pattern and gain. When compared to a flat plate reflector, a cup reflector can significantly reduce the back- and sidelobe levels of the pattern and can also enhance the gain of the helix, depending on the diameter and depth of the cup reflector. In the limit of large cup size, the resulting cup reflector transforms the helix into a helicone antenna [Carver, 1967].

The NEC models used by Emerson assumed a flat, infinite groundplane. While an infinite groundplane does eliminate any radiation in the hemisphere behind the helix, it does not account for the gain enhancement caused by the cup reflector. Emerson did examine models using finite groundplane of one and one-half wavelengths across using wire-grid mesh models, he found that there are little differences from those for the infinite groundplane cases. Thus, we should expect any simulation results that assume a flat planar reflector to under-estimate helix gains when compared to King and Wong's measured results as observed in Figure 3.16.

The theoretical model used by Lee and Wong [1982] made some simplifying assumptions about the current on the helix. They assumed that the smoothly decaying current in the feed region of the helix and the small amplitude reverse traveling on the helix could be ignored when computing the radiation fields of the helix. Thus, they considered the helix to only support a uniform amplitude, forward traveling wave. Based on models for the radiated fields of the helix they developed [Lee and Wong, 1982], they calculated the directivity of helices with the same parameters that King and Wong measured. Their efforts were an attempt to reconcile differences in gain measured by King and Wong and an earlier empirical gain expression for helix gain presented by Kraus [1988]. Kraus' empirical gain formula produced values greater than measured by King and Wong. Lee and Wong's theoretical results produced gain (directivity) values less than those measured by King and Wong as shown in Figure 3.16. As discussed above, Lee and Wong's model ignored some of the currents on the helix. In comparing their results to both King and Wong's measured results and Emerson's NEC simulations, it would appear that those the contributions of those currents are not insignificant after all.

In order to establish a baseline for our own simulations, we attempted to reproduce some of Emerson's results using NEC2 for modeling. Figure 3.17 shows a comparison of predicted gain for helices of 1, 2, and 3λ in axial length between our results and Emerson's results. Our results under predict the helix gain compared to Emerson's results. The differences vary with helix radius, but are generally less than 1 dB. We have investigated several issues that might account for these differences, but have come to no definitive conclusions. However, the two results are comparable at least qualitatively. We will use our simulation results in comparisons in following chapters with those of the Stub Loaded Helix with the implicit proviso that these results may be pessimistic when compared to the results of others.

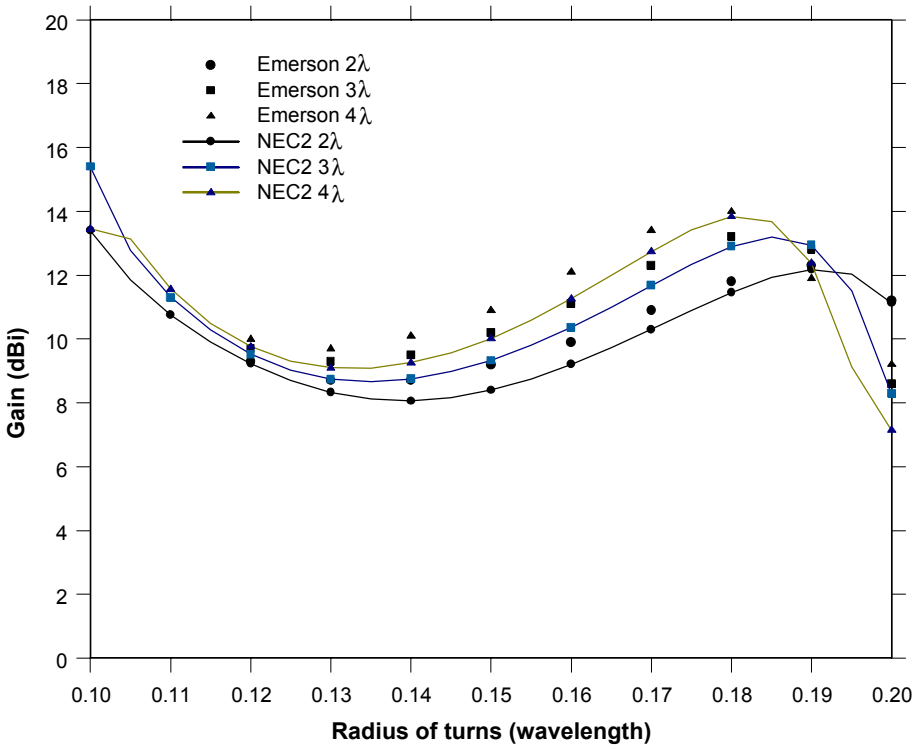

Figure 3.17 Comparison of predicted helix gain as a function of turn radius and axial length from NEC2 simulations to Emerson's [1994] results.